

AN X-RAY STUDY FOR WHITE DWARF BINARY AR SCORPII

J. TAKATA¹, X.F. WANG¹, H.H. WANG¹, L.C.-C. LIN², C.-P. HU³, K.L. LI⁴, AND A.K.H. KONG⁵

Draft version December 7, 2020

ABSTRACT

We report a study of the X-ray emission from the white dwarf/M-type star binary system AR Scorpii using archival data taken in 2016-2020. It has been known that the X-ray emission is dominated by the optically thin thermal plasma emission, and its flux level varies significantly over the orbital phase. The X-ray emission also contains a component that modulates with the beat frequency between the white dwarf's spin frequency and orbital frequency. In this new analysis, the 2020 data taken by NICER shows that the X-ray emission is modulating with the spin frequency as well as the beat frequency, indicating that part of the X-ray emission is coming from the white dwarf's magnetosphere. It is found that the signal of the spin frequency appears only at a specific orbital phase, while the beat signal appears over the orbital phase. We interpret the X-ray emission modulating with the spin frequency and the beat frequency as a result of the synchrotron emission from electrons with a smaller and larger pitch angle, respectively. In a long-term evolution, the beat pulse profile averaged over the orbital phase changed from a single-peak structure in 2016/2018 to a double-peak structure in 2020. The observed X-ray flux levels measured in 2016/2017 are higher than those measured in 2018/2020. The plasma temperature and amplitude of the orbital waveform might vary with time too. These results indicate that the X-ray emission from AR Scorpii evolves on a timescale of years. This long-term evolution would be explained by a super-orbital modulation related to, for example, a precession of the white dwarf, or a fluctuation of the system related to activity of the companion star.

1. INTRODUCTION

AR Scorpii is a binary system composed of a white dwarf (hereafter WD) and a M-type main-sequence star, and its distance from the Earth is estimated to be $d \sim 116$ pc (Marsh et al. 2016; Bailer-Jones et al. 2018; Peterson et al. 2019). The emission from radio to X-ray bands is modulating with the orbital period of $P_o \sim 3.56$ hours (Marsh et al. 2016; Stanway et al. 2018; Takata et al. 2018). Marsh et al. (2016) report that in addition to the orbital modulation, the radio/optical emission from AR Scorpii is modulating in a beat frequency, $\nu_b = \nu_s - \nu_o \sim 8.46$ mHz, where $\nu_s \sim 8.54$ mHz is the spin frequency of the WD and $\nu_o \sim 0.078$ mHz is the orbital frequency. AR Scorpii is the first WD that shows a modulation of the radio emission related to the WD's spin. The pulsed emission up to soft X-ray bands has been confirmed (Takata et al. 2018), and no confirmation of the GeV emission has been reported (Kaplan et al. 2019; Singh et al. 2020). A spin down of the WD has been measured by the optical observations (Marsh et al. 2016; Potter & Buckley 2018a; Stiller et al. 2018; Gaibor et al. 2020). With a longer base line of the optical observations, Gaibor et al. (2020) measure a spin down rate as $\dot{\nu}_s \sim (-4.82 \pm 0.18) \times 10^{-17}$ Hz s⁻¹, indicating the spin down power of $L_{sd} \sim 2 \times 10^{33}$ erg s⁻¹.

Marsh et al. (2016) report that the optical emission is minimum around the inferior conjunction of the companion star's orbit, where the companion star is between the WD and Earth, while it achieves the maximum level slightly earlier than the superior conjunction, where the companion star is behind the WD. Littlefield et al. (2017) find that the orbital modulation has been fairly stable with 78 days of observations, but suggest with a longer base line optical data that the orbital maximum shifts toward earlier phases relative to the superior conjunction with time. Katz (2017) interprets this observed orbital waveform and the long-term evolution with a precession model of the WD's spin axis. Peterson et al. (2019), on the other hand, report that the orbital waveform of AR Scorpii has remained constant across about one century, and constrain the first time derivative of the orbital frequency as $\dot{\nu}_o \leq 3.8 \times 10^{-20}$ Hz s⁻¹.

Marcote et al. (2017) carry out a radio observation with a high angular resolution and find that the radio emission region of AR Scorpii is compact with a scale of $\leq 4R_\odot$. They also report no evidence for a radio outflow or collimated jets. Then, Stanway et al. (2018) confirm that the orbital modulation in radio bands shows a similar trend to that of the optical emission. This indicates that inner-surface of the companion star is probably heated by an interaction with the WD magnetosphere or by an irradiation of synchrotron radiation from the WD's magnetosphere (Garnavich et al. 2019), and the emission from radio to optical bands is mainly produced at the region near or on the inner-surface.

The pulse profile folded with the beat frequency shows a double-peak structure in the radio, optical and UV bands. In optical/UV bands, the pulse shape can be described by a main peak plus a small secondary peak, for which the phase separation is ~ 0.5 (Marsh et al. 2016). The pulsed fraction reaches $> 95\%$ in the UV

takata@hust.edu.cn

¹ Department of Astronomy, School of Physics, Huazhong University of Science and Technology, Wuhan 430074, China

² Department of Physics, UNIST, Ulsan 44919, Korea

³ Department of Physics, National Changhua University of Education, Changhua 50007, Taiwan

⁴ Department of Physics, National Cheng Kung University, 70101 Tainan, Taiwan

⁵ Institute of Astronomy, National Tsing Hua University, Hsinchu 30013, Taiwan

band. Marsh et al. (2016) also find a signal of the spin frequency of the WD in the periodograms, suggesting that the optical pulsed emission originates from a region co-rotating with the WD. The optical emission from AR Scorpii is also unique with a strong linear polarization. Buckley et al. (2017) show that the degree of the linear polarization reaches up to $\sim 40\%$ at the pulse peak, and the position angle swings through 180° . These properties of the linear polarization indicate an origin of synchrotron emission from the relativistic electrons spiraling along the magnetic field of the WD (Potter & Buckley 2018b; Takata & Cheng 2019; du Plessis et al. 2019).

In radio bands, Marsh et al. (2016) show the pulse profile can be described by a double-peak structure with a pulsed fraction of $\sim 10\%$, which is smaller than those in the optical/UV bands. Stanway et al. (2018) report that the beat signal decreases with the radio frequency, and no beat signal is found at 1.5GHz. The radio emission does not show an evident signal of the WD spin in the periodograms, which indicates that the pulsed radio emission originates from the region in the magnetosphere of the companion star rather than in the magnetosphere of the WD. Stanway et al. (2018) also measure a weak linear polarization with a degree $< 1\%$ but a large circular polarization, which reaches to $\sim 30\%$ at the orbital phase $\phi_o \sim 0.8$, where $\phi_o = 0$ is defined at the inferior conjunction of the companion star's orbit. They suggest that a non-relativistic cyclotron emission dominates the radio emission at lower frequencies.

The broadband spectrum from the radio to UV bands can be described by a thermal optical emission from the companion star plus non-thermal component with a total luminosity of $L \sim 2 \times 10^{32}$ erg s $^{-1}$, which is about 10% of the spin down power. Garnavich et al. (2019) measure the slope of the optical spectrum and find that the power-law index s , $F_\nu \propto \nu^{-s}$, shows a significant variation in $0.8 < s < 2.0$ depending on the orbital phase and the optical brightness. They suggest that the variation in the power-law index is related to the synchrotron cooling and frequency of the replenishment of the energy injection. This non-thermal component has an energy peak at around 0.01eV and probably extends down to radio bands with a slope of $F_\nu \sim \nu^{1/3}$ (Stanway et al. 2018), which is consistent with the slope of low energy tail of the synchrotron emission (Geng et al. 2016). In the radio bands, the spectrum becomes shallower below ~ 1 GHz (Marsh et al. 2016; Stanway et al. 2018). This also indicates that an additional component (probably cyclotron emission from non-relativistic electrons) dominates at low radio frequency bands.

In the higher energy band, we (Takata et al. 2018) study the X-ray emission from AR Scorpii with an XMM-Newton observation carried out in 2016. The observed spectrum shows an iron-K line that is well described by an optically thin thermal plasma emission with several different temperatures; there is no signature of the emission from an accreting matter in the observed spectrum. The observed X-ray flux varies significantly over the orbital phase (Figure 1), and it achieves maximum and minimum at around the superior conjunction and inferior conjunction of the companion star, respectively. The hardness ratio of the observed X-ray emission, on the other hand, is almost constant over the orbital phase.

TABLE 1
JOURNAL OF THE OBSERVATION DATA USED IN THIS STUDY.

	Obs. ID	Date	Exposure (ks)	
XMM	0783940101	2016 Sep. 10	38.7	X16
-Newton	0795720101	2018 Feb. 19	30.0	X18
Chandra	19711	2017 June 23	26.1	Ch17
NuSTAR	30301027002	2018 Feb. 18	134.7	Nu18
NICER	3589010101	2020 June 14	5.6	
	3589010102	2020 June 14	19.3	
	3589010103	2020 June 16	15.4	Ni20
	3589010104	2020 June 16	9.5	
	3589010105	2020 June 18	6.9	

These emission properties are compatible to the thermal process of the plasmas heated to 0.1 – 10 keV on or near the inner surface of the companion star, and the orbital variation of the observed flux is caused by a variation of the visible emission region over the orbital phase rather than an absorption by the accretion column. The X-ray luminosity is of the order of $L_X \sim 4 \times 10^{30}$ erg s $^{-1}$, and it is $\sim 1\%$ of the optical/UV luminosity of the non-thermal component. Hence, a small fraction of the released energy is used for heating up the plasma to a temperature of \sim keV, and majority is for creating a population of the non-thermal electrons.

Takata et al. (2018) find a modulation with the beat frequency in the X-ray data below 2 keV. The pulse profile averaged over the orbital phase shows a single-peak (or probably double-peak with a small secondary peak). On the other hand, the orbital resolved analysis shows that the pulse structure evolves over the orbital phase, and the pulse profile at around the inferior conjunction of the companion star can be described by a double-peak structure with a prominent secondary peak. The averaged pulsed fraction is about 14%, suggesting that the unpulsed component is the main component in the X-ray bands. By comparing the pulse profile measured by the EPIC camera with the profile by the OM camera onboard XMM-Newton, we find that the X-ray peak and optical/UV peak are in phase. This suggests that the non-thermal component in optical/UV bands extends to the soft X-ray bands. The phase-resolved spectrum of the pulsed component in the 0.15-2 keV band shows evidence of the power-law component with a photon index $\Gamma = 2.3 \pm 0.5$ and an unabsorbed flux $F_{0.15-2} \sim 4 \times 10^{-13}$ erg cm $^{-2}$ s $^{-1}$.

After the discovery of the radio/optical pulsed emission from AR Scorpii in 2016, more X-ray data have been collected. It enables us to study a long-term evolution of the X-ray emission from AR Scorpii. In this paper, we study the X-ray emission properties of AR Scorpii using archival data taken by XMM-Newton, Chandra, NuSTAR and NICER during 2016-2020 (Table 1). In section 2, we summarize the data reduction for each observation. We present the results of the timing analysis in section 3 and of spectral analysis in section 4. In section 5, we discuss the X-ray emission process in the WD magnetosphere based on the results of the study.

2. DATA REDUCTION

2.1. XMM-Newton

We analyze the archival XMM-Newton data (MOS1/2 and PN) taken at 2016 September 10 (Obs. ID:0783940101, PI: Steeghs) and at 2018 February 19. (Obs. ID: 0795720101, PI: Pavlov) with total exposure times of 39 ks and 30 ks, respectively (Table 1). The observations were operated under the small window mode for the MOS1/MOS2 and the large window mode for the PN in 2016 (hereafter X16), while with full frame mode for all EPIC cameras in 2018 (hereafter X18). Event list for each detector and observation is produced in the standard way using XMM-Newton Science Analysis Software (XMMNAS, version 18.0.0). A point source is significantly detected by the XMMNAS task `detect_chain`. We generate the source spectra within a radius of 20'' circle centered at source position (R.A., Dec.)=(16^h21^m47^s.28, -22°53'10".4) and the background spectra from a source free region. When we generate the spectra, we remove epoch with background flaring by limiting the count rate above 10 keV to $< 0.35 \text{ count s}^{-1}$ for the MOS1/MOS2 data and $< 0.4 \text{ count s}^{-1}$ for the PN data. We create response files with the XMMNAS tasks `rmfgen` and `arfgen` with updated calibration files. We group the spectral bins to achieve a signal-to-noise ratio of $S/N \geq 3$ in each bin using the XMMNAS task `specgrp`. We use the XMMNAS task `barycen` to obtain barycenter corrected arrival times (ephemeris DE405) and create the background subtracted light curve with the task `epiclccorr` to examine the orbital variation. We generate the orbital light curves in the 0.3-10keV band, and compare it with the results of the Chandra and NICER data (Figure 1).

The X18 data recorded a large flare-like background event covering a significant part of the observation. After removing such a background event, the exposure of the data used in the spectral analysis is about 10 ks for the PN data and 20 ks for the MOS1/MOS2 data, respectively. Figure 2 shows the orbital phase distribution of the exposure time for the data used in the spectral analysis; the maximum exposure time is normalized to unity. We can see that a large exposure loss because of the background events causes a non-uniform orbital coverage of the X18 data. For the X16 data, the exposure loss due to the flare-like background events is less serious compared to the case of the X18 data.

2.2. Chandra

A Chandra observation for AR Scorpii (Obs. ID: 19711, PI:Pavlov) was operated under ACIS Timed Exposure (1/8 sub-array) mode and an exposure time of 24.8 ks (hereafter Ch17). We re-process the data with standard tasks in the CIAO Version 4.11. We use the CIAO task `specextract` to generate the source spectrum and associated response files from a circular region centered at aforementioned position with a radius 3.6'', and create a background spectrum from a vicinity source free region. It is known that pile-up of a Chandra data is significant when the count rate is $\geq 0.1 \text{ count s}^{-1}$ (Davis 2001). In section 4.1.3, we examine the pile-up fraction as $\sim 5\%$ for this observation. For a timing analysis, we apply the CIAO task `axbary` to obtain barycen-corrected arrival time of each event, and use `dmextract` task to create a background subtracted light curve in the 0.3-10keV band to examine the orbital variation. We check the background light curve and find no indication of flar-

ing. For searching a beat frequency in the data, we use the `Xselect` to extract events from the source region and obtain a photon count of ~ 4200 .

2.3. NuSTAR

To examine the hard X-ray emission from AR Scorpii, we analyze the archival NuSTAR data taken at 2018 February (Obs. ID: 30301027002, PI: Pavlov) with an exposure ~ 134 ks (hereafter Nu18). Event list and source/background spectra are produced in the standard way using `nupipeline` and `nuproducts` tasks of the `Heasoft`. Barycenter correction is applied in the `nuproducts` task. A point source is clearly seen in the generated image. We create the source spectrum with the data extracted from a circular region with a radius of 50'' centered at aforementioned source position, and we obtain a background spectrum from a vicinity source free region. We use `grppha` task of the FTTOOLS to group the spectral bins such that new grouping contains a minimum of 30 counts in each bin. We create a background subtracted light curve in the 3-78 keV band. We extract $\sim 10,000$ events from the source region, and search for the beat frequency in the data.

2.4. NICER

NICER observed AR Scorpii at 2020 June 14-16 (Obs. IDs: 589010101-358901015 PI: Mori) with a total exposure ~ 57 ks (hereafter Ni20). We merge the `mpu7_ufa` files for the five observations using the task `nimpmerge` of the `Heasoft`, and screen the data using the tasks `nicerclean` and `nimaketime`. We filter the raw data with the standard criteria for analysis of the beat/spin modulation, and we apply an additional filtering based on the magnetic cut-off rigidity to generate spectrum and orbital light curve. We accept the time with $> 1.5\text{GeV}/c$ in current analysis and find that a more tight filtering does not affect much to the result of the analyses. We use the latest calibration files (`xiti20200722`) and recalibrate the energy scale using the file `nixtiflightpi20170601v004.fits`. We apply a barycentric time correction to the created event list using `barycor` task of the `Heasoft`. After standard screening, we also remove flare-like background events using the `Xselect`.

We generate the spectra of the source region and background modeling with `nibackgeng3C50` task implemented in the `HEASoft`; we create a filter file with an option `coltypes="base,3c50"` in the task `niprefilter2`⁶. We use the `grppha` task to group the generated spectrum such that new grouping contains a minimum of 40 counts in each bin. We note that the best-fit parameters for the spectrum obtained with the original event file is consistent with those obtained with the `nibackgeng3C50` product within the errors. In this study, therefore, we will present the fitting result with the `nibackgeng3C50` product.

Figure 2 shows that the 2020 NICER observation does not cover uniformly the orbital phase. We generate an exposure corrected light curve in the 0.3-10 keV band using the `Xselect`. Using the source and background spectra obtained by the `nibackgeng3C50` task, we estimate that the background emission contributes to $\sim 55\%$

⁶ <https://heasarc.gsfc.nasa.gov/lheasoft/ftools/headas/niprefilter2.html>

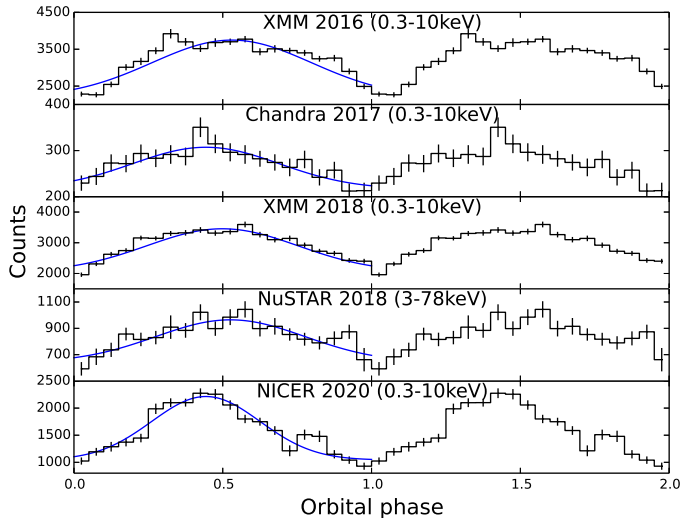


FIG. 1.— Orbital modulation measured by each data set. Background contribution is subtracted and exposure loss for each bin is corrected (Figure 2). For Ni20 data, we assume the background level as 55% of the total emission in the 0.3-10 keV band (section 2.4). The blue solid curve in each panel represents the best-fit function with one Gaussian component plus a constant component.

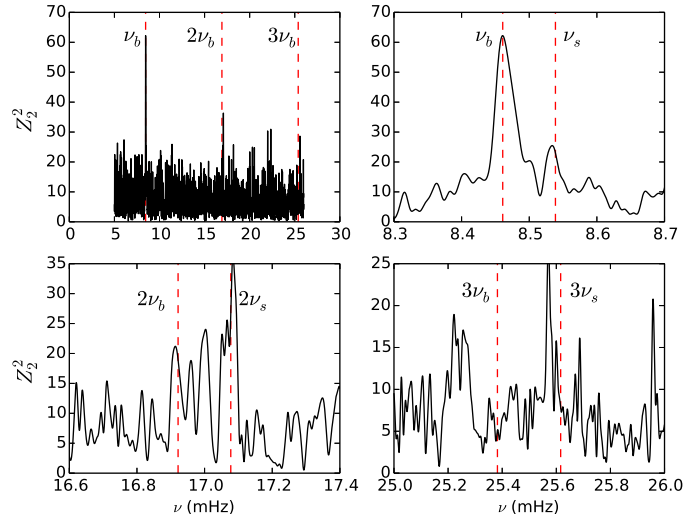


FIG. 3.— Z_2^2 periodogram for the XMM-Newton 2018 data. ν_b and $\nu_s = \nu_b + 0.0792\text{mHz}$ represents the beat frequency and spin frequency of the WD, respectively.

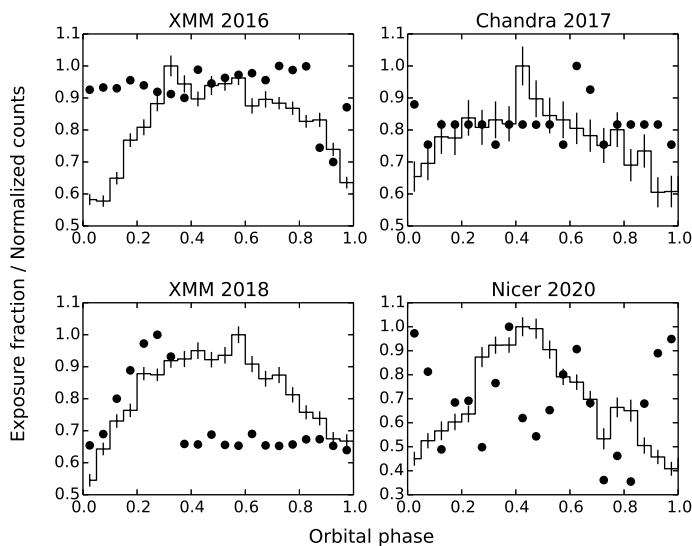


FIG. 2.— Distribution of the exposure fraction (filled circles) over the orbital phase. Histograms shows the orbital variation after correction of the exposure loss. For X18 data, the large exposure loss in the orbital phase $\phi_o = 0.4 - 1$ is caused by large flare-like background events. For Ni20 data, a non-continuous monitoring of the source produces a large fluctuation of the exposure fraction over the orbital phase.

of total emission in the 0.3-10 keV band. By removing 55% of the total counts from the generated light curve, we create a background subtracted light curve, which is compared with other observations (Figure 1).

3. TIMING ANALYSIS

3.1. Properties of the orbital modulation

We create folded light curve with the orbital ephemeris reported by Marsh et al. (2016): $\nu_o = 0.077921380$ mHz

and $T_0(\text{MJD}) = 57264.09615$ when the companion star is located at the inferior conjunction. Figure 1 shows the orbital light curves in the 0.3-10 keV band for the X16/18, Ch17 and Ni20 data and in the 3-78 keV band for the Nu18 data; the background level is subtracted for each light curve. We can see that all light curves show a significant orbital modulation, and the observed flux levels achieve the maximum and minimum at around the superior conjunction ($\phi_o = 0.5$) and inferior conjunction ($\phi_o = 0$), respectively. As discussed in Takata et al. (2018), this pattern of the orbital modulation indicates that X-ray emission from AR Scorpii mainly originates from the region located near or on the inner surface of the companion star.

To examine a long-term evolution of the orbital waveform, we fit the obtained light curve with one Gaussian component plus a constant component (Figure 1). We define amplitude of the orbital variation as $(f_{max} - f_{min}) / (f_{max} + f_{min})$, where f_{max} and f_{min} are the maximum and minimum counts obtained from the best-fit function, respectively (Inam et al. 2004; Rea et al. 2007). We obtain amplitudes of $\sim 0.22 \pm 0.01$ for the X16 data, $\sim 0.16 \pm 0.03$ for the Ch17 data, $\sim 0.21 \pm 0.01$ for the X18 data and $\sim 0.18 \pm 0.02$ for the Nu18 data. For the Ni20 data, we obtain an amplitude of $\sim 0.32 \pm 0.01$ by assuming 55% of the background level, and we find that the amplitude is larger than those of other data. This would provide evidence of the long-term evolution of the orbital waveform in the X-ray bands, although additional observations with an imaging capability is necessary to confirm it. By comparing the amplitude of X18 data with that of Nu18 data, we find less dependency of the orbital waveform on the photon energy. This constant amplitude among different energy bands also indicates that the orbital modulation is caused by a variation of the visible emission region over the orbital phase.

3.2. Searching for pulsation

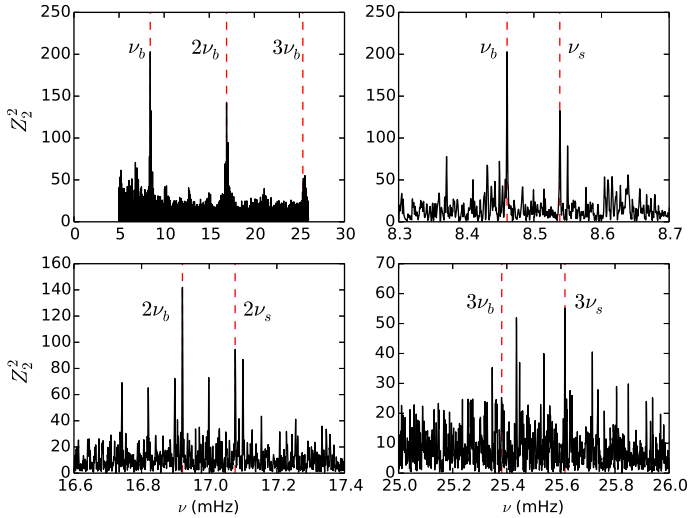


FIG. 4.— Z_2^2 periodogram for the NICER 2020 data. ν_b and ν_s represents the beat frequency and spin frequency of the WD, respectively.

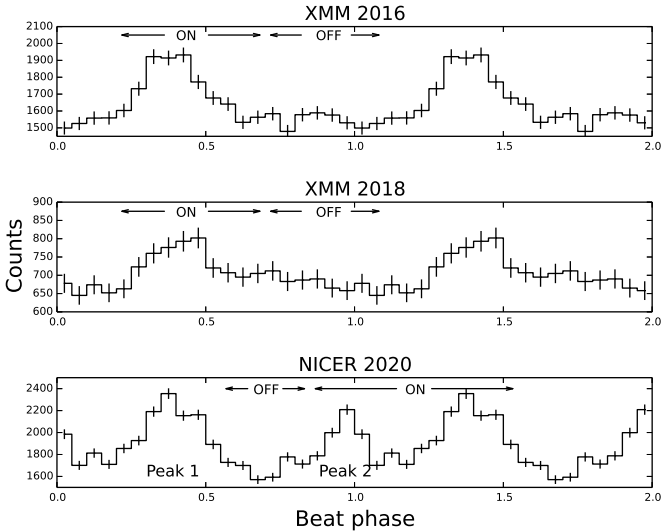


FIG. 5.— Pulse profiles in the 0.3-2 keV band folded with the beat frequency for the three data sets. Each event is folded with the timing solution described in section 3.3, and the background contribution is subtracted for each light curve. The 55% of the background level in the total emission is assumed for Ni20 data. “ON” and “OFF” in each panel indicate the on-pulse phase and off-pulse phase to generate the spectrum of the pulsed component, respectively (section 4.3).

We search the beat frequency $\nu_b \sim 8.6\text{mHz}$ (Marsh et al. 2016) using the Z_2^2 -test (Buccheri et al. 1983). For the X16 and X18 data sets, the extracted photon events from the source region yield $\sim 45,000$ and $\sim 20,000$ counts, respectively. We use $\sim 4,200$ counts for Ch17, $\sim 10,000$ counts for Nu18 FPMA/FPMB and $\sim 135,000$ photons for Ni20 to search the beat frequency. In addition to the X16 data reported by Takata et al. (2018), a significant pulsed signal is found in X18 and Ni20 data sets. Since the pulsed fraction is $\sim 14\%$ (Takata et al. 2018), the counts of the pulsed emission

in the Ch17 data will be only ~ 600 or less, and it is unlikely to find a beat signal in the data. Although we combine all observations, which include the Nu20 data, to search a pulsation in the > 2 keV band, we do not find any significant signal at the beat frequency. This non-detection of the beat frequency with the number of the collected photon counts is expected, because only $\sim 2\%$ of the total emission from AR Scorpii is pulsating in the > 2 keV band (section 4.3).

Figures 3 and 4 present the Z_2^2 -periodograms for the X18 and Ni20 data, respectively [see Takata et al. (2018) for the Z_2^2 periodogram of the X16 data]. We can see a strong signal at the beat frequency $\nu_b \sim 8.46\text{mHz}$ and the 1st harmonic in the Ni20 data. In addition to the beat frequency, we can also confirm a significant signal at the spin frequency of the WD, $\nu_s \sim 8.53\text{mHz}$ and the 1st/2nd harmonics. The signal of the spin frequency with $Z_2^2 \sim 125$ of the Ni20 data is much stronger than $Z_2^2 \sim 50$ of the X16 data (Takata et al. 2018) and $Z_2^2 \sim 20$ of the X18 data. The Ni20 data therefore provides a concrete evidence that the pulsed X-ray emission originates from the WD magnetosphere and its emission region is co-rotating with the WD.

3.3. Long-term evolution of pulse profile

To compare between the pulse profiles measured by XMM-Newton and NICER observations, we restrict the photon energy in the 0.3-2 keV band, and create folded light curves with the beat ephemeris provided by Gaibor et al. (2020): $\nu_b = 8.460297018\text{mHz}$, $\dot{\nu}_b = -4.82 \times 10^{-17}\text{Hz s}^{-1}$ and $T_0(\text{MJD}) = 57941.16888790$. For X16/18 data, we determine the background level from a nearby source free region. For Ni20 data, we generate the background subtracted light curve by assuming that the background level is 55% of the total emission.

Figure 5 shows the pulse profiles for the three data sets, and we find that the pulse profile of the Ni20 data is significantly different from those of the X16/18 data. The pulse profiles of the X16/X18 data show a single-peak structure. For the Ni20 data, on the other hand, the pulse profile shows a double-peak structure with a phase separation of $\delta\phi_b \sim 0.4 - 0.5$. The difference in the pulse profiles between the X16/X18 and Ni20 data may indicate a temporal evolution of the pulsed X-ray emission. Takata et al. (2018), on the other hand, find that the pulse profile evolves over the orbital phase, and it can be represented by either a single peak structure or a double-peak structure. The pulse profile obtained with all data of each observation therefore may depend on how the observation covers the orbital phase. In fact, we can see a large fluctuation of the exposure time over the orbital phase for the Ni20 data (Figure 2).

We examine the orbital evolution of the pulse profiles to investigate the cause of the difference between the pulse profiles of the X16/18 and Ni20 data. Figure 6 is a dynamic pulse profile folded with the beat frequency over the orbital phase using the X16 data (left panel) and the Ni20 data (right panel); the pulse profile at each orbital phase is created with the data of successive 0.1 orbital phase, and the total count (area of the profile) is normalized to unity. We can see that the dynamic pulse profiles in two data sets are similar to each other, except for feature of the secondary peak appeared at the

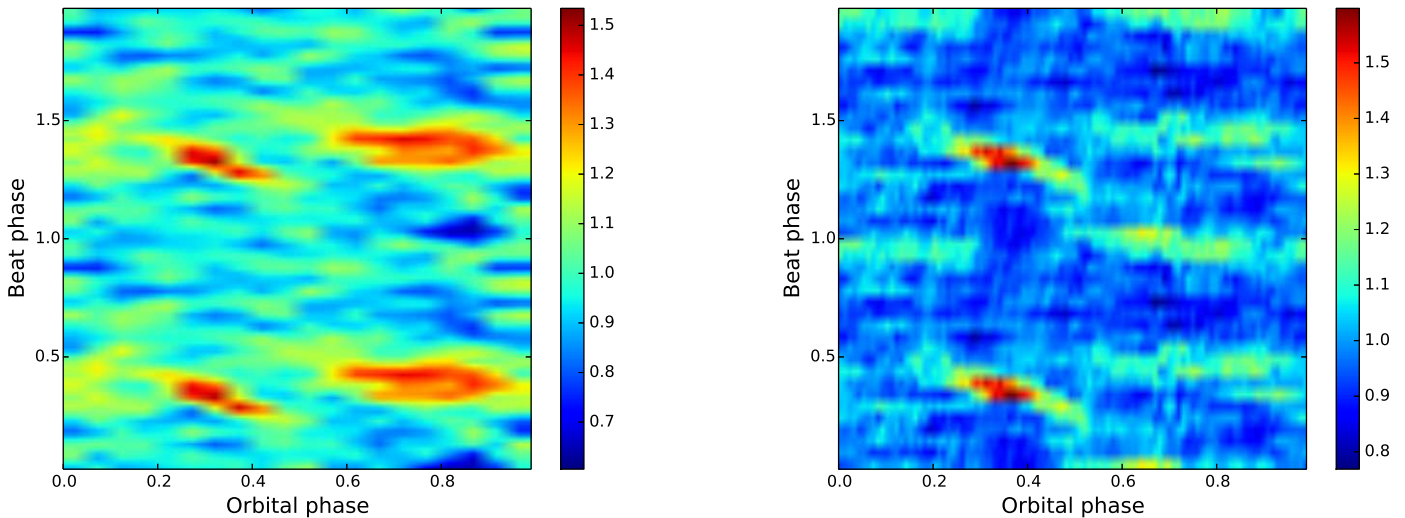


FIG. 6.— Dynamic pulse profiles in the 0.3-2 keV band for X16 (left) and Ni20 (right) data. The data is folded with the beat phase and the pulse profile at each orbital phase is created by the data of successive 0.1 orbital phase. Total count (area of the profile) of each pulse profile is normalized to unity.

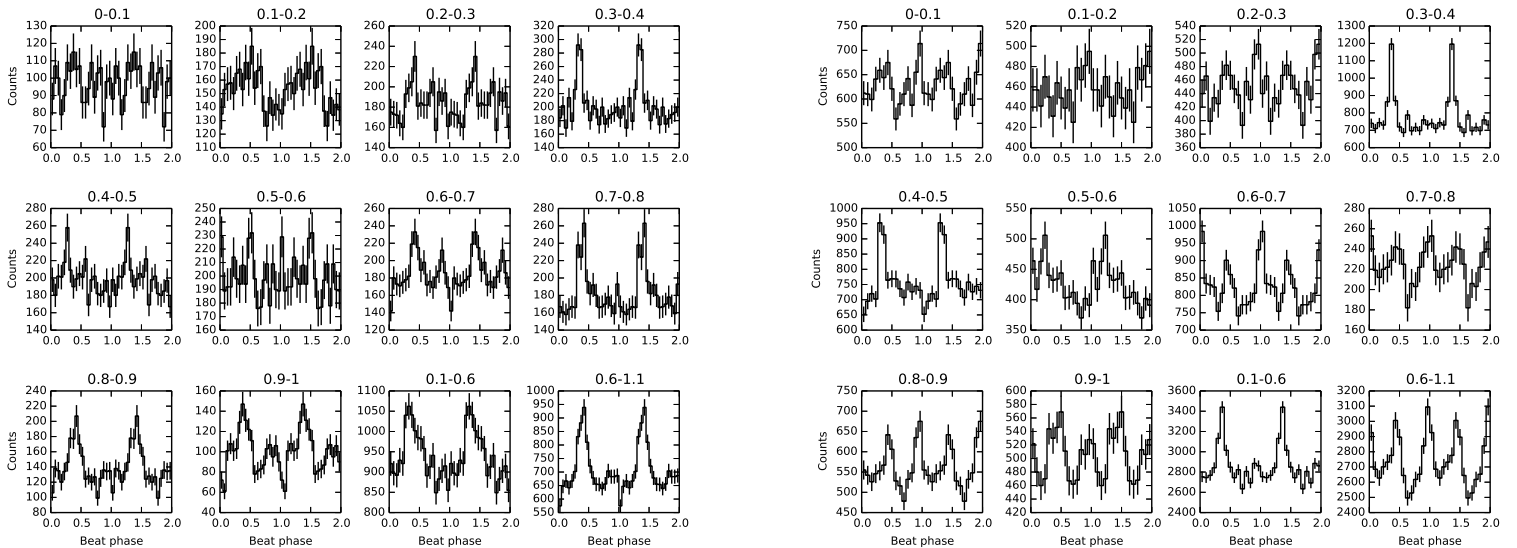


FIG. 7.— Orbital resolved pulse profiles in the 0.3-2 keV band for X16 (left) and Ni20 (right) data. Bottom right two panels show the pulse profiles in the phase segments $\phi_o = 0.1 - 0.6$ and $0.6 - 1.1$, respectively.

beat phase $\phi_b \sim 0$ (equivalently $\phi_b \sim 1$) and during the orbital phase $\phi_o \sim 0.5 - 1$.

Figure 7 shows the orbital resolved pulse profiles for the X16 (left) and Ni20 (right) data. In both data sets, the pulse profile at the orbital phase $\phi_o \sim 0.3$ can be described by a single-peak structure appeared at the beat phase $\phi_b \sim 0.5$. Then the peak position migrates to earlier beat phase during the orbital phase $\phi_o \sim 0.3 - 0.6$, as the dynamic pulse profiles indicate. After the orbital phase $\phi_o > 0.6$, we can see a double peak structure in both the X16 and Ni20 data. For the X16 data, the original peak at the beat phase $\phi_b \sim 0.5$ always dominates the secondary peak at $\phi_b \sim 0$. For Ni20 data, on the other hand, the secondary peak has a similar or larger

intensity compared to the original peak. In the bottom row of the figure, we present the pulse profiles integrated over the orbital phase $\phi_o = 0.1 - 0.6$ and $\phi_o = 0.6 - 1.1$, respectively. We find in the figure that the pulse profiles in $\phi_o = 0.1 - 0.6$ for the X16 and Ni20 both can be described by a single-peak structure. For $\phi_o = 0.6 - 1.1$, on the other hand, the pulse profile of the Ni20 data shows a double-peak structure with a secondary peak stronger than the original peak. For the Ni20 data, we can see that the pulse profile averaged over the orbital phase using the normalized pulse profiles presented in Figure 6 is also described by the double-peak structure. These results therefore suggest that the difference between the pulse profiles of the X16/X18 data and Ni20 data is an

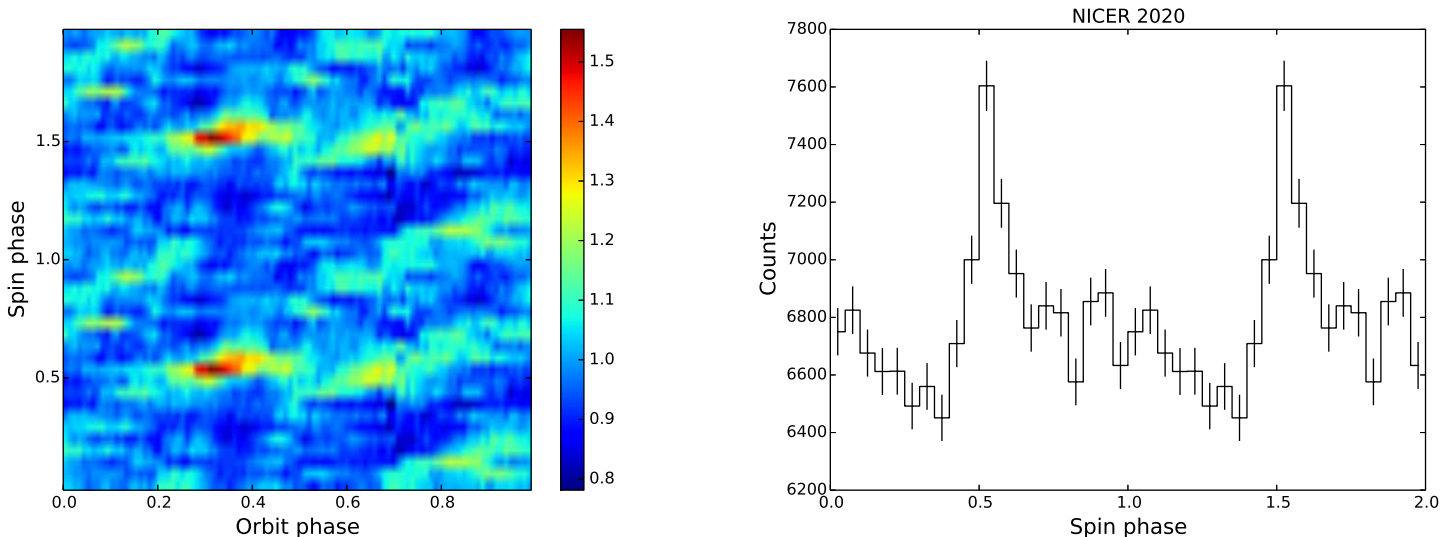


FIG. 8.— Left: Dynamic pulse profile folded with the spin frequency for Ni20 data set. Right: Pulse profiles in the 0.3-2 keV band folded with the spin frequency for Ni20 data set.

intrinsic feature, and the pulsed X-ray emission experiences a long-term evolution.

We define the pulsed fraction with the equation, $(f_{max} - f_{min}) / (f_{max} + f_{min})$, with f_{max} and f_{min} being the maximum and minimum counts in the light curve. In 0.3-2.0 keV bands, we obtain 0.13 ± 0.02 for X16, 0.11 ± 0.03 for X18, and 0.20 ± 0.02 for Ni20 data, respectively. We find that the pulsed fraction of the Ni20 data is higher than those of the X16/X18 data. The pulsed fraction may show a long-term evolution, as well as the structure of the pulse profile. Although we could not find the pulsed emission above 2 keV bands, we estimate a pulsed fraction less than 2% on the basis of the spectral analysis (section 4.3).

3.4. Mixture between spin and beat modulations

In the dynamic pulse profile in Figure 6, we can see that a migration of the pulse peak position at the orbital phase $\phi_o \sim 0.2 - 0.5$. This migration suggests an existence of a signal with another period. In fact, the Z_2^2 periodogram for the Ni20 data (Figure 4) clearly indicates that a component of the X-ray emission from AR Scorpii modulates with not only the beat frequency but also the WD's spin frequency. Figure 8 presents dynamic pulse profile folded with the spin frequency (left panel) and integrated pulse profile (right panel) of the Ni20 data. In the dynamic pulse profile, we can see a relatively constant peak position in the spin phase during the orbital phase $\phi_o \sim 0.2 - 0.5$. This suggests that the signal of the WD's spin frequency appears in the X-ray data only at a specific orbital phase interval. As the right panel in Figure 8 shows, the spin pulse profile integrated over the orbital phase can be described by a single peak structure, which is different from the double-peak structure of the beat pulse profile.

We divide the Ni20 data into two orbital intervals, $\phi_o = 0.1 - 0.6$ and $\phi_o = 0.6 - 1.1$, and perform the Z_2^2 -test for each interval (Figure 9). The periodogram of the orbital phase $\phi_o = 0.1 - 0.6$ shows the signal of the spin frequency that is stronger than the signal of the

beat frequency. During $\phi_o = 0.1 - 0.6$, moreover, we can see a strong signal at the average of two frequencies (dotted vertical lines), and the first harmonics of the averaged frequency has a power stronger than those of the $2\nu_b$ and $2\nu_s$ in the periodogram. This supports the fact that the short-term modulation during $\phi_o = 0.1 - 0.6$ is caused by the mixture between the beat frequency and spin frequency. For $\phi_o = 0.6 - 1.1$ (right panel in Figure 9), on the other hand, no signal of the spin frequency is found in the Z_2^2 periodogram, and the short-term modulation is dominated by the beat frequency. We find that the first harmonic of the beat frequency during the orbital phase $\phi_o = 0.6 - 1.1$ shows a Z_2^2 power similar to or stronger than the power of the fundamental frequency. This is consistent with the double-peak structure with a phase separation ~ 0.5 appeared in the pulse profile folded with the beat frequency.

We note that the dynamic pulse profile of the X16 data (left panel in Figure 6) also shows a migration of the peak position and therefore indicates an appearance of the spin frequency at the orbital phase interval $\phi_o \sim 0.2 - 0.5$. The similar behavior of the X16 and N20 data suggests that the appearance of signal of the WD's spin frequency only at a specific orbital phase interval is regularly repeated by every orbit. In section 5, we discuss the mixture between the spin and beat frequencies in the short-term modulation and its dependency on the orbital phase.

4. SPECTRAL ANALYSIS

The spectrum of the X-ray emission from AR Scorpii can be described by an optically thin thermal plasma emission with several different temperatures (Takata et al. 2018). In this study, we fit the generated spectra with a multi-temperature VMEKAL model (Mewe et al. 1985, 1986) using Xspec version 12.10.1f. We apply TBABS model for modeling photoelectric absorption.

4.1. Analysis for individual data set

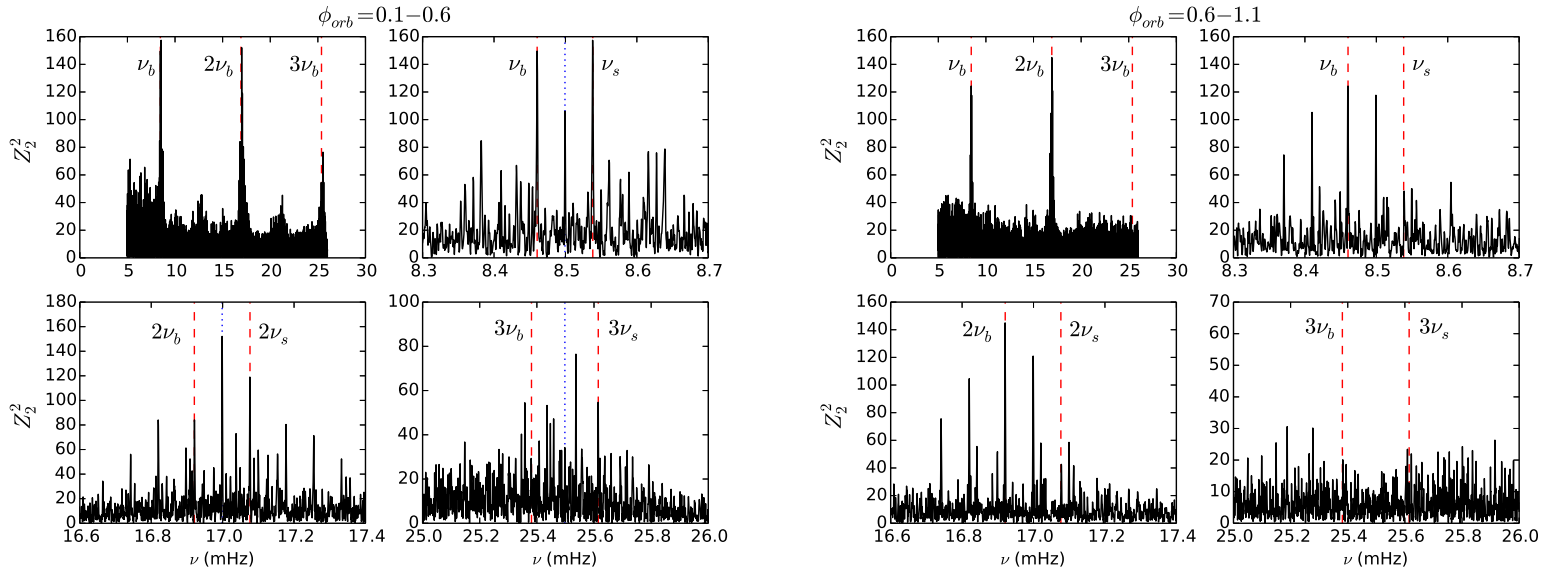


FIG. 9.— Orbital resolved Z_2^2 periodogram for Ni20 data set. ν_b and ν_s represents the beat frequency and spin frequency of WD, respectively. The dotted lines in the left panel show the position of the average between two frequencies.

TABLE 2
FITTINGS FOR 2016 XMM-NEWTON DATA (0.2-12 KEV BANDS) WITH
THREE-TEMPERATURE VMEKAL MODELS.

	Takata et al. (2018) ^a	Model 1 ^a	Model 2 ^b
N_H (10^{20} cm^{-2})	$3.4^{+0.8}_{-0.8}$	$1.2^{+0.3}_{-0.2}$	$2.8^{+0.5}_{-0.5}$
F_e	$0.67^{+0.29}_{-0.21}$	$0.45^{+0.07}_{-0.07}$	$0.28^{+0.06}_{-0.05}$
kT_1 (keV)	$8.0^{+2.8}_{-1.6}$	$7.6^{+6.0}_{-1.9}$	$6.3^{+1.3}_{-1.0}$
kT_2 (keV)	$1.7^{+0.4}_{-0.3}$	$2.4^{+0.9}_{-0.7}$	$1.5^{+0.2}_{-0.2}$
kT_3 (keV)	$0.6^{+0.1}_{-0.1}$	$0.63^{+0.04}_{-0.05}$	$0.32^{+0.04}_{-0.03}$
χ^2_{red} (dof)	1.03 (404)	1.20 (406)	1.08 (406)

^a Except for iron, the abundances are fixed to the solar abundances [Anders and Grevesse (1989)]

^b The abundances of O, Ne, Mg, S and Si are linked to that of Fe.

4.1.1. Reanalysis for X16 data

Although Takata et al. (2018) fit the spectrum of the X16 data with a three-temperature VMEKAL model, we reanalyze the data with the updated calibration files of XMM-Newton observation. Table 2 compares the best-fit parameters reported in Takata et al. (2018) with those in the new analysis. In Takata et al. (2018) (the second column), a reasonable fit is obtained by thawing iron (Fe) abundance and by fixing other elements to the solar abundance. In our new analysis, however, we find that the reduced χ^2 of the fitting with the model (Model 1 in third column) becomes worse comparing to the previous result, and the best-fit parameters show a smaller hydrogen column density (N_H).

To find a better fitting model, we thaw each element step by step. We find that abundances of another five elements (O, Ne, Mg, S and Si) smaller than the solar abundance significantly improve the fitting results with a F statistic value of 8.2, which means that the probability of this improvement being caused by chance is 2.3×10^{-7} . Since the predicted abundances of those components are consistent with that of the iron within the errors, Table 2

(Model 2) shows the best-fit parameters by linking the abundances between the iron and the five elements. We find that the hydrogen column density and two higher temperatures are consistent with previous result, but the abundance of the Fe and the lowest temperature decrease from the previous one.

4.1.2. NICER data

Since NICER has no imaging capability, we check whether the spectra obtained with the process described in section 2.4 is indeed consistent with the X-ray emission from AR Scorpii. We restrict the photon energy in the 0.3-2 keV band for the spectral analysis of the NICER data because of strong background contamination in lower/higher energy bands. We use the Model 2 of Table 2, in which the abundances of O, Ne, Mg, S, Si and Fe elements are linked. We find that the background subtracted spectrum is reasonably fitted by a two-temperature VMEKAL model with the best-fit hydrogen column density $N_H = 4.6^{+0.8}_{-0.7} \times 10^{20} \text{ cm}^{-2}$, temperatures $kT_1 = 2.6^{+0.4}_{-0.4}$ keV and $kT_2 = 0.67^{+0.09}_{-0.06}$ keV ($\chi^2_{red} = 1.15$ for 163 dof: third temperature component is not necessary). The Fe abundance of $0.27^{+0.11}_{-0.08}$ (solar abundance) is consistent with the result of the X16 data in Table 2. A simple black-body radiation model or a power-law model cannot provide a reasonable fit. Hence, the generated spectrum likely represents the X-ray emission from AR Scorpii.

The pulse profiles folded with the beat frequency of the Ni20 data shows a single-peak structure in $\phi = 0.1 - 0.6$ and a double-peak structure in $\phi = 0.6 - 1.1$ (Figure 7). We therefore create the orbitally resolved spectra for $\phi_o = 0.1 - 0.6$ and $\phi_o = 0.6 - 1.1$, and we check any orbital evolution of the best-fit parameters with the two-temperature VMEKAL model. We do not find a significant difference in the best-fit parameters of two orbital phase intervals. This is not unexpected because the pulsed emission is only $\sim 10\%$ of the total emission, and

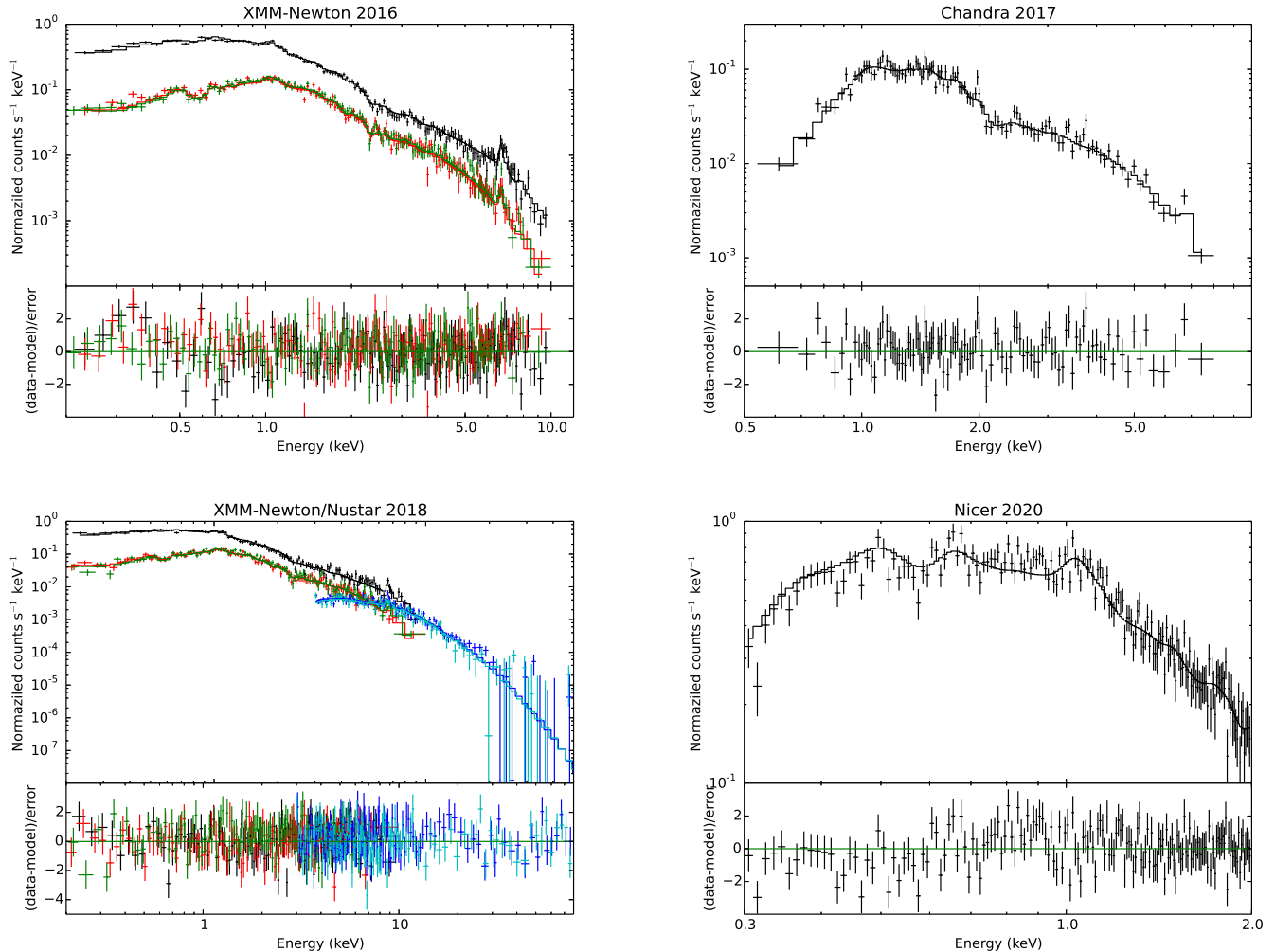


FIG. 10.— X-ray spectrum of AR Scorpii. Top left: 2016 XMM-Newton observation. The black, red and green correspond to PN, MOS1 and MOS2, respectively. Top right: 2017 Chandra observation. Bottom left: 2018 XMM-Newton/NuSTAR observations. For XMM-Newton data, the black, red and green show the spectra of PN, MOS1 and MOS2, respectively. For NuSTAR data, the blue and cyan correspond to FPMA and FPMB data, respectively. Bottom right: 2020 NICER observation.

the spectrum is dominated by the un-pulsed component.

4.1.3. Pile-up fraction of Chandra data

First, we use the *Web PIMMS* Version 4.11 to estimate pile-up fraction of the Chandra data. Since the *Web PIMMS* implements the APEC⁷ model for the plasma emission, we fit the generated spectrum with a two-temperature APEC model with the *Xspec*. Since the data cannot constrain the hydrogen column density, we fix it at $N_H = 3.0 \times 10^{20} \text{cm}^{-2}$. A reasonable fit is obtained with the temperatures $kT_1 = 5.1_{-0.5}^{+1.2}$ keV, $kT_2 = 1.0_{-0.3}^{+0.4}$ keV and the iron abundance $0.6_{-0.3}^{+0.2}$ ($\chi_{red}^2 = 1.0$ for 107 dof). With the frame time of the observation, 0.8 s, the *Web PIMMS* estimates the pile-up fraction as ~ 5 percent. Second, we use the CIAO’s fitting package, *Sherpa*, to estimate the pile-up fraction. We fit the spectrum with a two-temperature VMEKAL components plus pile-up model (Davis 2001). The fitting result shows the plasma temperatures $kT_1 = 4.1_{-0.5}^{+0.5}$ keV,

$kT_2 = 0.8_{-0.4}^{+0.3}$ keV and abundance Fe = $0.67_{-0.13}^{+0.14}$. The estimated pile-up fraction is ~ 5 percent (so called α -parameter and f -parameter are ~ 0.8 and 0.89 , respectively), which is consistent with the result of the *Web PIMMS*.

4.1.4. Joint fitting for X18 and Nu18 data

The observations for the X18 and Nu18 data were carried out on 2018 February 18 and 19, respectively. This joint observation enables us to investigate X-ray spectrum of AR Scorpii over a wide energy range in the 0.2–78keV bands. In particular, we can investigate the behavior of the X-ray spectrum above 10keV bands. We perform a joint fit for the two spectra by introducing a **constant** factor to account for cross-calibration mismatch between the XMM-Newton and NuSTAR observations. During the fitting process, we fix the **constant** factor for the X18 data at unity, and obtain a constant factor of ~ 1.1 for the Nu18 data.

First we fit the spectrum with a three-temperature VMEKAL model (Model 2 in Table 3), in which we link the abundances of six elements (O, Ne, Mg, S, Si and Fe)

⁷ <http://atomdb.org/>

TABLE 3
JOIN FITTING FOR THE SPECTRA (0.2-78 KEV BANDS) OF
2018 XMM-NEWTON AND NUSTAR OBSERVATIONS.

	Model 2	Model 3 ^a	Model 4 ^b
N_H (10^{20}cm^{-2})	$4.0^{+2.1}_{-1.4}$	$3.4^{+1.6}_{-1.1}$	$2.6^{+0.6}_{-0.6}$
F_e	$0.22^{+0.05}_{-0.05}$	$0.28^{+0.08}_{-0.08}$	$0.31^{+0.07}_{-0.06}$
kT_1 (keV)	$6.8^{+0.8}_{-0.6}$	$4.1^{+0.4}_{-0.4}$	$2.7^{+0.3}_{-0.3}$
kT_2 (keV)	$1.5^{+0.2}_{-0.2}$	$0.82^{+0.07}_{-0.07}$	$0.66^{+0.14}_{-0.09}$
kT_3 (keV)	$0.34^{+0.32}_{-0.06}$	-	-
α^c	-	$1.6^{+0.1}_{-0.3}$	$-0.20^{+0.5}_{-1.0}$
E_c^d (keV)	-	-	$4.2^{+1.9}_{-1.1}$
χ_{red}^2 (dof)	1.07 (546)	1.14 (546)	1.07 (545)

^a Two VMEKAL + Power-law model.

^b Two VMEKAL + Power-law plus exponential cut-off model.

^c Photon index of the power-law component.

^d Cut-off energy of the power-law plus cut-off component.

and obtain the best-fit parameters as $N_H = 4.0^{+2.1}_{-1.4} \times 10^{20}\text{cm}^{-2}$, $kT_1 = 6.8^{+0.8}_{-0.6}$ keV, $kT_2 = 1.5^{+0.2}_{-0.2}$ keV, $kT_3 = 0.34^{+0.32}_{-0.06}$ and $F_e = 0.22^{+0.05}_{-0.05}$ with $\chi_{red}^2 = 1.07$ for 546 dof., which are consistent with the results of X16 data within the errors (Table 2).

To examine the spectral behavior above 10keV bands, we replace one VMEKAL component to a power-law model, and fit the spectrum with `constant*tbabs*(vmekal+vmekal+powerlaw)` (Model 3 in Table 3). We obtain the best-fitting photon index of $\alpha = 1.6^{+0.1}_{-0.3}$, but we find that the $\chi_{red}^2 \sim 1.14$ of the fitting becomes worse in comparison to the three-temperature VMEKAL model. This would suggest that the observed spectrum does not extend in the hard X-ray band with a single power-law form.

Finally we consider possibility of a spectral cut-off feature by replacing the power-law component to a power-law plus an exponential cut-off model. We fit the data with `constant*tbabs*(vmekal+vmekal+cutoffpl)` (Model 4 in Table 3), and obtain an acceptable fit with $\chi_{red}^2 \sim 1.07$ for 545 dof, which is comparable to that of three VMEKAL model. The best-fit parameters, however, show a very hard photon index of $\alpha \sim -0.20^{+0.5}_{-1.0}$ with a cut-off energy $E_c \sim 4.2^{+1.9}_{-1.1}$ keV, and indicate that the spectrum of the third component in higher energy band has a convex shape. This spectral property is consistent with a thermal emission rather than a non-thermal emission, and therefore the optically thin thermal plasma emissions with three different temperatures describes better the X-ray emissions from AR Scorpii over the 0.2-78keV bands.

4.2. Investigation for long-term evolution

We fit all spectra of X16, Ch17, X18/Nu18 and Ni20, simultaneously, with a three-temperature VMEKAL model by linking the hydrogen column densities in different data sets. We apply the pile-up model implemented in the Xspec, and fit all spectra with the model `pileup*constant*tbabs*(vmekal+vmekal+vmekal)`, for which we turn on the pile-up model only for the Chandra data. Since the pile-up parameters α and f are not constrained by the current data, we fix the those parameters to be the best-fit values 0.8 and 0.89,

TABLE 4
SIMULTANEOUS FITTINGS FOR THE SPECTRA (0.2-78 KEV BANDS)
WITH THREE-TEMPERATURE VMEKAL MODELS AND BY LINKING
THREE TEMPERATURES.

	X16	Ch17	X18/Nu18	Ni20
N_H (10^{20}cm^{-2})			$3.8^{+0.4}_{-0.4}$	
F_e			$0.25^{+0.03}_{-0.03}$	
kT_1 (keV)			$6.4^{+0.6}_{-0.4}$	
kT_2 (keV)			$1.4^{+0.19}_{-0.05}$	
kT_3 (keV)			$0.30^{+0.02}_{-0.02}$	
N_1^a (10^{-4})	$12.7^{+0.5}_{-1.0}$	$13.1^{+1.0}_{-1.0}$	$11.0^{+0.6}_{-1.1}$	$8.4^{+0.8}_{-0.9}$
N_2^a (10^{-4})	$5.0^{+1.3}_{-0.7}$	$6.9^{+1.6}_{-1.5}$	$5.3^{+1.3}_{-0.8}$	$4.6^{+0.9}_{-0.8}$
N_3^a (10^{-4})	$2.5^{+0.4}_{-0.4}$	$1.6^{+1.4}_{-1.4}$	$1.6^{+0.4}_{-0.4}$	$0.8^{+0.2}_{-0.2}$
$F_{0.3-10}^b$	$2.88^{+0.03}_{-0.03}$	$3.05^{+0.09}_{-0.09}$	$2.54^{+0.04}_{-0.04}$	$1.97^{+0.03}_{-0.03}$
χ_{red}^2 (dof)			1.12 (1232)	

^a Normalization of the VMEKAL component in units of $10^{-14}/(4\pi d^2) \int n_e n_H dV$, where d (cm) is the distance to the source.

^b Unabsorbed flux in the 0.3-10 keV band in units of 10^{-12} erg $\text{s}^{-1}\text{cm}^{-2}$.

TABLE 5
SIMULTANEOUS FITTING FOR THE SPECTRA (0.2-78 KEV BANDS)
WITH THREE-TEMPERATURE VMEKAL MODELS AND BY UNLINKING
LOWER TWO TEMPERATURES.

	X16	Ch17	X18/Nu18	Ni20
N_H (10^{20}cm^{-2})			$3.6^{+0.4}_{-0.3}$	
F_e			$0.26^{+0.03}_{-0.03}$	
kT_1 (keV)			$6.8^{+0.6}_{-0.5}$	
kT_2 (keV)	$1.6^{+0.1}_{-0.2}$	$1.6^{+0.6}_{-0.3}$	$1.6^{+0.2}_{-0.2}$	$1.6^{+0.3}_{-0.2}$
kT_3 (keV)	$0.29^{+0.02}_{-0.02}$	$0.3^{+0.7}_{-0.2}$	$0.32^{+0.07}_{-0.04}$	$0.61^{+0.08}_{-0.11}$
N_1 (10^{-4})	$11.8^{+1.0}_{-1.0}$	$11.9^{+1.6}_{-2.5}$	$10.1^{+1.1}_{-1.1}$	$7.6^{+1.6}_{-2.0}$
N_2 (10^{-4})	$6.0^{+1.1}_{-1.1}$	$8.0^{+2.6}_{-2.2}$	$6.2^{+1.3}_{-1.3}$	$4.9^{+1.9}_{-1.6}$
N_3 (10^{-4})	$2.2^{+0.4}_{-0.3}$	$1.7^{+100.0}_{-1.4}$	$1.4^{+0.4}_{-0.3}$	$1.0^{+0.3}_{-0.2}$
$F_{0.3-10}$	$2.86^{+0.03}_{-0.03}$	$3.05^{+0.09}_{-0.09}$	$2.51^{+0.04}_{-0.04}$	$1.93^{+0.04}_{-0.04}$
χ_{red}^2 (dof)			1.09 (1226)	

respectively, obtained in section 4.1.3. The `constant` factors for the X16, Ch17, X18 and Ni20 data are fixed to unity. We link the abundances of the six elements (O, Ne, Mg, S, Si and Fe) and fix other elements to the solar abundances, as discussed in section 4.1.1. A long-term evolution of the spectral properties is discussed with following three cases.

First, by assuming a constant plasma temperature and flux with time, we link the three temperatures and normalization factors for all data sets. We find that the fitting model is unacceptable with a reduced chi-square of $\chi_{red}^2 \sim 2.3$ for 1232 dof. Then we unlink the normalization factors, but keeping the linking for the temperatures. We obtain a reasonable fit with $\chi_{red}^2 \sim 1.12$ for 1216 dof. Table 4 and Figure 10 summarize the best-fit parameters and spectra, respectively. We find that the best-fit parameters are consistent with the results of the fitting for the X16 data only (Model 2 in Table 2). In Table 4, we can see that the 0.3-10 keV unabsorbed flux deviates from a constant flux with time. One possibility is an intrinsic temporal evolution of the X-ray emission of AR Scorpii as indicated by the evolution of the pulse profile discussed in section 3. For example, we can see

TABLE 6
FITTINGS FOR 2016 AND 2018 XMM-NEWTON DATA (0.2-12KEV BANDS)
WITH THREE-TEMPERATURE MEKAL MODELS.

	2016		2018	
	0-0.35/0.85-1	0.35-0.85	0-0.35/0.85-1	0.35-0.85
N_{H} (10^{20} cm^{-2})			$2.9^{+0.5}_{-0.4}$	
F_e^{b}			$0.27^{+0.05}_{-0.04}$	
kT_1 (keV)			$7.0^{+1.5}_{-1.2}$	
kT_2 (keV)			$1.6^{+0.1}_{-0.2}$	
kT_3 (keV)			$0.32^{+0.04}_{-0.02}$	
N_1 (10^{-4})	$10.3^{+1.5}_{-1.2}$	$12.3^{+1.7}_{-1.4}$	$9.9^{+1.4}_{-1.2}$	$10.4^{+1.7}_{-1.4}$
N_2^{a} (10^{-4})	$5.6^{+1.6}_{-1.9}$	$6.5^{+1.8}_{-2.1}$	$5.1^{+1.6}_{-1.7}$	$6.7^{+1.9}_{-3.0}$
N_3^{a} (10^{-4})	$1.4^{+0.4}_{-0.3}$	$2.2^{+0.5}_{-0.4}$	$1.2^{+0.4}_{-0.4}$	$1.1^{+0.5}_{-0.5}$
$F_{0.3-10}^{\text{c}}$	$2.53^{+0.04}_{-0.04}$	$3.03^{+0.04}_{-0.04}$	$2.38^{+0.05}_{-0.05}$	$2.62^{+0.06}_{-0.06}$
χ_{red}^2 (dof)			0.99 (1229)	

in Table 4 that the normalization factors (N_1 , N_2 and N_3) of the Ni20 data are smaller than the values of the X16 data, indicating the volume of the emission region evolves with time.

We also unlink the abundances for the different data sets to see how the best-fit parameters evolve. We obtain the best-fit abundances as $F_e = 0.21 \pm 0.04$ for X16, $0.33^{+0.22}_{-0.15}$ for Ch17, 0.22 ± 0.04 for X18/Nu18 and $0.54^{+0.18}_{-0.13}$ for Ni20, respectively. The abundance of Ni20 data is higher than those of the other data sets. This may be due to the fact that the spectrum of Ni20 is limited in the 0.3-2.0 keV bands, which does not cover the 6.8 keV line emission from He-like F_e , and hence the abundance of Fe may be overestimated. We can see that other best-fit parameters are consistent with the results in Table 4 within the errors.

Second, to investigate another possibility that the change of the X-ray flux is associated with a change of the temperature of the emitting plasmas, we re-fit the data by unlinking the lower two temperature components (kT_2 and kT_3). For the highest temperature, since the Ch17 and Ni20 data sets cannot constrain the value, we keep the linking. An improvement of the fitting is found with a F static value 5.5, which means that the probability of this improvement being caused by chance is $\sim 10^{-5}$. Table 5 summarizes the best-fit parameters of this model. The X16, Ch17 and X18/Nu18 data are consistent with a constant temperature, although the error range for kT_2 of Ch17 is large. We find however that the lowest temperature $kT_3 \sim 0.61$ keV of the Ni20 data is higher than the values $kT_3 \sim 0.3$ keV of the other data sets, suggesting the plasma temperature shows a temporal evolution. We find that this tendency of the temperatures does not change, even though we unlink the abundances for the different data sets. In such a case, we obtain the abundances of $F_e = 0.25 \pm 0.05$ for X16, $0.50^{+0.28}_{-0.23}$ for Ch17, 0.23 ± 0.05 for X18/Nu18, and $0.45^{+0.18}_{-0.12}$ for Ni20, respectively.

Finally, we can see in Figure 2 that the different observations were carried out with a different exposure distribution over the orbital phase. Since the observed X-ray emission shows an orbital modulation with a large amplitude, it is possible that the different coverage over the orbit produces an apparent long-term evolution of the flux. To investigate such a possibility, we check orbital

phase-resolved spectra for the X16 and X18 data. As we can see in Figure 2, the exposure distribution at the orbital phase $\phi_o \sim 0.35 - 0.85$ is relatively uniform for both X16 and X18 data sets. Hence, we divide the orbital phase into two intervals, $0 - 0.35/0.85 - 1$ and $0.35 - 0.85$, and obtain a spectrum for each orbital interval.

Table 6 summarizes the best-fit parameters with a three-temperature VMEKAL model; we link the temperatures of the two data sets and the abundances for 6 elements (O, Ne, Mg, S, Si and Fe). In each observation, we find that the flux in $\phi_o = 0.35 - 0.85$ is higher than that in $\phi_o = 0 - 0.35/0.85 - 1$, and the flux averaged over the two phase intervals is consistent with the flux obtained from the whole data of each observation (Table 4). In each orbital phase interval, the flux of the X16 data is higher than that of the X18 data. These results suggest that the difference in the exposure distribution over the orbital phase is not the main reason of the difference between the fluxes of the X16 and X18 data sets. Although more concrete evidence is required with more data, the non-pulsed X-ray emission, as well as the pulsed emission, of AR Scorpii likely experiences a long-term evolution on a timescale of years.

4.3. Pulsed spectrum

Takata et al. (2018) examine the spectrum of the pulsed component with the X16 data and find evidence of a power-law component with a photon index $\Gamma = 2.3 \pm 0.5$. In the new analysis, we include the X18 and Ni20 data set, but exclude MOS1/MOS2 data of the X16/X18 data because of a small amount of the photon counts. We define the on-pulse phase and off-pulse phase based on the pulse profiles folded with the beat frequency, and we generate the spectrum of the pulsed component by subtracting the off-pulse spectrum from the on-pulse spectrum. As indicated in Figure 5, we define the on-pulse phase to cover the main peak for the X16/18 data, and to cover main/secondary peaks for the Ni20 data. We generate on-pulse and off-pulse spectra using the XMMAS for the X16/X18 data and using the Xselect for the N20 data. We use the grppha task to group the spectral bins so that the count in each bin after subtracting the off-pulse emission remains >40 photons for the X16/X18 data and >100 photons for the Ni20 data.

During the fitting, we fix the hydrogen column den-

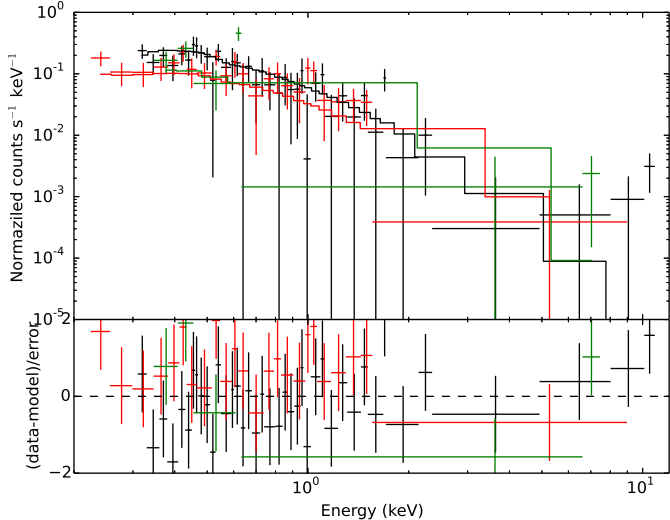


FIG. 11.— Spectrum of the pulsed component. The red, green and black point/model show the X16, X18 and Ni20 data sets, respectively.

sity at $N_H = 3.5 \times 10^{20} \text{ cm}^{-2}$ inferred from the phase averaged spectrum. The power-law model provides a reasonable fit with a photon index of $\Gamma = 2.80^{+0.28}_{-0.25}$ ($\chi^2_{red} = 0.8$) and an unabsorbed flux of $F_{0.2-2 \text{ keV}} = 2.37^{+0.29}_{-0.28} \times 10^{-13} \text{ erg cm}^{-2}\text{s}^{-1}$. Such a large photon index is consistent with a slope expected from the ratio of the fluxes in optical and X-ray bands. An optically thin plasma emission model (e.g. two-temperature MEKAL model) also provides a comparable goodness of the fit with temperatures $kT_1 = 1.8^{+1.5}_{-1.3} \text{ keV}$ and $kT_2 = 0.11^{+0.03}_{-0.08} \text{ keV}$, but we cannot constrain the abundance. The black-body radiation model predicts an emission size of $\sim 0.1 \text{ km}$ with a source distance $d \sim 0.1 \text{ kpc}$, which is unreasonably small.

Garnavich et al. (2019) find that the photon index of the optical emission varies significantly with the orbital phase and with the emission magnitude. With the current X-ray data quality, however, it is difficult to investigate such a dependency of the properties of the pulsed emission on the beat phase or on the orbital phase.

As discussed in section 3, we cannot find the beat signal in the $> 2 \text{ keV}$ band. If the spectrum of the pulsed emission could extend beyond 2 keV band with a power-law distribution, the expected flux in the $2\text{-}10 \text{ keV}$ band is $F_{2-10 \text{ keV}} = 3.2^{+1.2}_{-0.8} \times 10^{-14} \text{ erg cm}^{-2}\text{s}^{-1}$, which is $\sim 2\%$ of the total emission in the $2\text{-}10 \text{ keV}$ band. Using all data sets, we have a total of $\sim 55,000$ events in the $> 2 \text{ keV}$ band. Since the background emission dominates in the $> 2 \text{ keV}$ band of the Ni20 data, the events related to the pulsed emission will be much less than $\sim 1,100$. With current collected photon counts, therefore, the significance of the pulsation in the $> 2 \text{ keV}$ band will be too small to be detected (i.e., $< 5\sigma$), even if the power-law component extends to that energy band.

5. SUMMARY AND DISCUSSION

We have studied the X-ray emission from AR Scorpii with the archival data taken in 2016-2020. In the short-

term modulation, the periodogram using the Ni20 data clearly indicates a modulation of the spin frequency of WD, indicating that part of the X-ray emission is coming from the WD's magnetosphere. The short term modulation during the orbital phase $\phi_o \sim 0.1 - 0.6$ is caused by the mixture between the beat frequency and the spin frequency, while the intensity peak during $\phi_o \sim 0.6 - 1.1$ is regularly repeated with the beat frequency. The X16 data also indicates such a modulation behavior over the orbital phase. Hence, the appearance of the WD's spin frequency in the X-ray emission only at the specific orbital phase is repeated by every orbit. In the long-term variation, we find that the observed flux level in 2016/2017 was higher than those measured in 2018/2020, and the amplitude of the orbital waveform of the 2020 NICER data might be larger than those of other data sets taken in 2016-2018. Moreover, the beat pulse profile averaged over the orbital phase changed from a single-peak structure in 2016/2018 to a double-peak structure in 2020. These results suggest that the X-ray emission from AR Scorpii experiences a long-term evolution on a timescale of years. The spectrum of the pulsed emission can be fit by a power-law function with a photon index $\Gamma \sim 0.25 - 0.31$.

A mixture of the beat frequency and the spin frequency in the short-term modulation is also observed in the optical emission from AR Scorpii (Marsh et al. 2016; Potter & Buckley 2018a,b). According to the figure 3 in Potter & Buckley (2018b) (the periodogram of the optical data), the beat signal is much stronger than the spin signal in the optical band. In the X-ray bands, the signal of the WD's spin frequency during the orbital phase $\phi_o \sim 0.1 - 0.6$ is similar strength to or may be stronger than that of the beat frequency, while the signal of the spin frequency disappears during the orbital phase $\phi_o \sim 0.6 - 1, 1$, as we discussed in section 3. This shows that a component of the X-ray emission modulating with the WD spin frequency appears and disappears in the observation over the orbital phase. We may interpret the signal of the beat frequency and the spin frequency in the X-ray emission as a result of the synchrotron emission from two kind of the electron populations characterized by a larger and a smaller pitch angles, respectively. A brief discussion of this interpretation is as follows.

We assume a non-thermal emission process for the observed X-ray emission modulating with the spin and/or beat frequencies. The non-thermal process of AR Scorpii has been discussed that an interaction between the magnetosphere of the WD and companion star may form a bow shock or cause a magnetic dissipation process, which could accelerate the electrons from the companion star (Geng et al. 2016; Buckley et al. 2017; Takata et al. 2017; Singh et al. 2020). Garnavich et al. (2019) and Lyutikov et al. (2020), on the other hand, propose that it is related to the magnetic reconnection event in the magnetosphere of the WD because of the interaction with the flow from the companion star. Bednarek (2018) proposes a hadronic model, in which the electrons and protons are accelerated in a strongly magnetized turbulent region around the M-type star, and the primary electrons and/or secondary electron/positron pairs produce a non-thermal emission from AR Scorpii. We assume that the accelerated electrons at the interaction region are trapped in the WD magnetosphere and, produce the

non-thermal emission through the synchrotron radiation.

The modulation of the beat frequency has been interpreted that the energy and/or particle injection for the synchrotron radiation is enhanced when the magnetic pole points toward the companion star (Geng et al. 2016; Potter & Buckley 2018b). Takata et al. (2017) suggest on the other hand that the synchrotron emission around the magnetic mirror points, where the pitch angle of the electrons becomes 90 degree, produces a pulsed emission. In their model, if the WD's magnetic pole is inclined from the spin axis, the electrons injected into the WD's magnetosphere at different spin/beat phases migrate to the first magnetic mirror points with different travel times. With the effect of the travel times, the emission from different magnetic mirror points can enhance the observed intensity at certain spin/beat phase, and results in the formation of the pulse. This model expects that the pulse profile evolves over the orbital phase, because the position of the WD relative to the companion star measured from the Earth depends on the orbital phase.

In the observed X-ray emission, the modulation with the WD's spin frequency appears only at a specific orbital phase interval. Potter & Buckley (2018b) discuss synchrotron radiation from a region fixed in the WD's magnetosphere to explain the optical pulsed emission from AR Scorpii. They demonstrate that by choosing an appropriate pitch angle of the synchrotron radiation, the pulsed emission modulating with the spin frequency appears brighter during the orbital phase $\phi_o \sim 0.2 - 0.45$ only, because of a beaming effect of the synchrotron radiation. Our speculative interpretation therefore is that the pulsed X-ray emission of AR Scorpii are produced by two kinds of the electron populations; electrons having a larger pitch angle and one having a smaller pitch angle. The emission that modulates with the beat frequency is produced by the population with a larger pitch angle, while the emission that modulates with the spin frequency is produced by the population with a smaller pitch angle.

The electrons that are injected from the interaction region will initially move toward the WD surface along the magnetic field line. Because of the conservation of the first adiabatic invariance, the pitch angle increases as the electrons approach to the WD surface, because the strength of the magnetic field increases. If the electrons with a pitch angle θ_0 are injected into the WD magnetosphere at a radius distance a from the WD, the pitch angle will evolve with the radial distance, r , measured from the WD as

$$\sin \theta(r) = \left(\frac{a}{r}\right)^{3/2} \sin \theta_0, \quad (1)$$

where we assume a magnetic dipole field and ignore a change of the Lorentz factor due to the synchrotron radiation loss. The electrons injected with a larger pitch angle will lose their energy at or near the magnetic mirror point. Since the emission from the electrons with a larger pitch angle covers a wider area in the sky, it can be observable over the orbital phase. We expect that such an emission modulates with the beat frequency.

For the electrons injected with a smaller pitch angle, on the other hand, they can move in the deeper WD's magnetosphere while keeping a small pitch angle. If the magnetic field is strong enough, the electrons may lose their

energy through the synchrotron radiation before reaching the magnetic mirror points. A simple quantitative estimation is the following. As an electron moves along the dipole magnetic field line toward the WD, the synchrotron loss timescale (τ_{syn}) decreases since the pitch angle and magnetic field strength increase. When the synchrotron loss timescale becomes of the order of the dynamic timescale, $\tau_c = r/c$, the electrons significantly lose the energy. By equating $\tau_{syn} = \tau_c$, and using the equation (1), we estimate the Lorentz factor of the electron (i) that are injected with a pitch angle θ_0 at $r = a$ and (ii) that emit the typical synchrotron photon energy E_{syn} as

$$\gamma = \frac{2}{3} \left[\frac{16\pi}{27} r_e^{9/16} r_g^{-1/8} R_{WD}^{3/8} a^{3/16} \left(\frac{E_{syn}}{hc} \right) \right]^{16/23} \sin^{2/23} \theta_0, \quad (2)$$

where $r_e = e^2/m_e c^2$ and $r_g = m_e c^2 R_{WD}^3 / (e \mu_{WD})$ with μ_{WD} and R_{WD} being the dipole moment and radius of the WD, respectively. The radial distance, r_s , at the emission region and the pitch angle at r_s become

$$r_s = \left[\frac{16\pi}{27} r_e^2 r_g^{-3} R_{WD}^9 a^{9/2} \left(\frac{E_{syn}}{hc} \right) \right]^{2/23} \sin^{6/23} \theta_0, \quad (3)$$

and

$$\sin \theta(r_s) = \left[\frac{16\pi}{27} r_e^2 r_g^{-3} R_{WD}^9 a^{-7} \left(\frac{E_{syn}}{hc} \right) \right]^{-3/23} \sin^{14/23} \theta_0, \quad (4)$$

respectively.

We may apply $\mu_{WD} = 5 \times 10^{34}$ G cm³ and $R_{WD} = 10^9$ cm for the WD parameters of AR Scorpii (Buckley et al. 2017), and $a = 8 \times 10^8$ cm of the separation between centers of two stars as the injection distance (since the companion star, whose radius is $\sim 2 \times 10^{10}$ cm, occupies a large portion of the space between centers of the two stars, this distance of the injection may be a crude approximation). Then, if the initial pitch angle is very small, for example $\sin \theta_0 = 0.01$, we obtain $\gamma \sim 9000$, $\sin \theta(r_s) \sim 0.06$ and $r_s = 2 \times 10^{10}$ cm, respectively, for the photon energy $E_{syn} = 1$ keV. Such an electron therefore loses the energy while keeping the small pitch angle. The emission from the small pitch angle approximately directs along the magnetic field line, and it is observable by the observer whose line of sight is parallel to the direction of the magnetic field at the radial distance r_s . We expect that the X-ray emission from such a small pitch angle is observed only at a specific spin phase interval (like the pulsar emission) and hence the observed emission modulates with the spin frequency.

The detectability of the emission from a small pitch angle for AR Scorpii will depend on the orbital phase because of the beaming effect. We assume that new high-energy electrons on a WD's magnetic field line are injected when the magnetic field line interacts with the companion star magnetosphere/outflow. Since the dynamical timescale (\sim one second) and the synchrotron timescale at the emission point are much shorter than the WD's spin period, we anticipate that, in terms of the spin phase, the ejected electrons immediately lose most of their energy after the injection. At a specific orbital phase interval, therefore, if there is no electron injection when the magnetic field at the distance r_s directs toward

the observer, we cannot observe the X-ray emission modulating with the WD's spin. This beaming effect could explain why the signal of the WD's spin frequency in the observed X-ray emission appears and disappears over the orbital phase.

Finally, another unique property is that AR Scorpii shows a long-term evolution of the X-ray emission. In particular, the X-ray light curve folded with the beat frequency clearly indicates an evolution of the pulsed component on a time-scale of years. This evolution could be caused either by an fluctuation or secular evolution of the state of the system. The change of the pulse profile and orbital modulation have been discovered in the X-ray emission from an intermediate polar (IP), XY Arietis (Norton & Mukai 2007), which is the accreting magnetic white dwarf, and the observed X-ray emission mainly originates from the white dwarf surface hit by the accretion flow. XY Arietis experienced an outburst because of a substantial increase of the accretion rate in 1996 (Hellier et al. 1997), and the increase of the mass transfer was probably caused by a result of a thermal-viscous disk instability (Hameury & Lasota 2017) or an enhancement mass transfer rate from the companion star. Hellier et al. (1997) report that the spin pulse profile evolved from a double-peaked profile to a single-peaked profile during the outburst. Norton & Mukai (2007) find that the spin pulse profile and the orbital waveform of XY Arietis also show a long-term evolution in the quiescent state. They interpret the long-term evolution in quiescent state with a precession model of an accretion disk.

AR Scorpii is a different type of WD's binary system from the IP in the sense that there is no accretion disk in the system and the pulsed X-ray emission is likely produced by the synchrotron radiation of the relativistic electrons in the WD's magnetosphere. It has been expected that the modulation peak in the beat phase occurs when the magnetic poles direct toward the companion star. The double peak structure of the Ni20 data (and optical data) with a phase separation ~ 0.5 implies the emission from the northern and southern hemispheres. The single-peak structure observed in the X16

and X18 data may indicate that the X-ray emission from one hemisphere in 2016/2018 was intrinsically dim because of an anisotropic energy injection from the interaction region. If this interpretation is true, the emerging secondary peak in the Ni20 data might be due to an increase of the energy injection to the hemisphere.

Another possible interpretation can be that the X-ray emission from one hemisphere was geometrically invisible in 2016/2018 observations, and it became visible in 2020. This interpretation could be possible if the spin axis of the WD is precessing. Schwarzenberg-Czerny (1992) estimate the precession period would be $\sim 10^4 - 10^5$ times the WD's spin period, which depends on the oblateness of the star. Katz (2017) applies the precession model to explain the orbital waveform in the optical bands, and predicts a precession period of 20-200 years for AR Scorpii. Tovmassian et al. (2007, 2012) report an evidence of the WD's precession in the X-ray emission from two IPs. If this precession scenario is true for AR Scorpii, the transition between a single-peak and a double-peak structures in the pulse profile folded with the beat frequency will be regularly repeated with the precession frequency. Since the pulse peak in the X-ray bands is aligned with the peak in the optical/UV bands, more long-term multi-wavelength observations will be required to understand the origin of the long-term evolution of the emission from AR Scorpii.

We thank to referee for his/her useful comments and suggestions. J.T., W.X.F and W.H.H. are supported by the National Science Foundation of China (NSFC) under 11573010, 11661161010, U1631103 and U1838102. L.C.C.L. is supported by NRFK through the grant number of 2016R1A5A1013277. K.L.L. is supported by the Ministry of Science and Technology of the Republic of China (Taiwan) through grants 108-2112-M-007-025-MY3 and 109-2636-M-006-017, and he is a Yushan (Young) Scholar of the Ministry of Education of the Republic of China (Taiwan). AKHK is supported by the Ministry of Science and Technology of the Republic of China (Taiwan) through grants 108-2628-M-007-005-RSP and 109-2628-M-007-005-RSP.

REFERENCES

- Bailer-Jones, C. A. L., Rybizki, J., Fouesneau, M., Mantelet, G., & Andrae, R. 2018, *AJ*, 156, 58
- Bednarek, W. 2018, *MNRAS*, 476, L10
- Buccheri, R., Bennett, K., Bignami, G. F., et al. 1983, *A&A*, 128, 245
- Buckley, D. A. H., Meintjes, P. J., Potter, S. B., Marsh, T. R., & Gänsicke, B. T. 2017, *Nature Astronomy*, 1, 0029
- Davis, J. E. 2001, *ApJ*, 562, 575
- du Plessis, L., Wadiasingh, Z., Venter, C., & Harding, A. K. 2019, *ApJ*, 887, 44
- Gaibor, Y., Garnavich, P. M., Littlefield, C., Potter, S. B., & Buckley, D. A. H. 2020, *MNRAS*, 496, 4849
- Garnavich, P., Littlefield, C., Kafka, S., et al. 2019, *ApJ*, 872, 67
- Geng, J.-J., Zhang, B., & Huang, Y.-F. 2016, *ApJ*, 831, L10
- Hameury, J. M., & Lasota, J. P. 2017, *A&A*, 602, A102
- Hellier, C., Mukai, K., & Beardmore, A. P. 1997, *MNRAS*, 292, 397
- Inam, S. Ç., Baykal, A., Matthew Scott, D., Finger, M., & Swank, J. 2004, *MNRAS*, 349, 173
- Kaplan, Q., Meintjes, P. J., Singh, K. K., et al. 2019, arXiv e-prints, arXiv:1908.00283
- Katz, J. I. 2017, *ApJ*, 835, 150
- Littlefield, C., Garnavich, P., Kennedy, M., et al. 2017, *ApJ*, 845, L7
- Lyutikov, M., Barkov, M., Route, M., et al. 2020, arXiv e-prints, arXiv:2004.11474
- Marcote, B., Marsh, T. R., Stanway, E. R., Paragi, Z., & Blanchard, J. M. 2017, *A&A*, 601, L7
- Marsh, T. R., Gänsicke, B. T., Hümmelich, S., et al. 2016, *Nature*, 537, 374
- Mewe, R., Gronenschild, E. H. B. M., & van den Oord, G. H. J. 1985, *A&AS*, 62, 197
- Mewe, R., Lemen, J. R., & van den Oord, G. H. J. 1986, *A&AS*, 65, 511
- Norton, A. J., & Mukai, K. 2007, *A&A*, 472, 225
- Peterson, E., Littlefield, C., & Garnavich, P. 2019, *AJ*, 158, 131
- Potter, S. B., & Buckley, D. A. H. 2018a, *MNRAS*, 478, L78
- . 2018b, *MNRAS*, 481, 2384
- Rea, N., Nichelli, E., Israel, G. L., et al. 2007, *MNRAS*, 381, 293
- Schwarzenberg-Czerny, A. 1992, *A&A*, 260, 268
- Singh, K. K., Meintjes, P. J., Kaplan, Q., Ramamonjisoa, F. A., & Sahayanathan, S. 2020, *Astroparticle Physics*, 123, 102488
- Stanway, E. R., Marsh, T. R., Chote, P., et al. 2018, *A&A*, 611, A66
- Stiller, R. A., Littlefield, C., Garnavich, P., et al. 2018, *AJ*, 156, 150
- Takata, J., & Cheng, K. S. 2019, *ApJ*, 875, 119
- Takata, J., Hu, C. P., Lin, L. C. C., et al. 2018, *ApJ*, 853, 106
- Takata, J., Yang, H., & Cheng, K. S. 2017, *ApJ*, 851, 143
- Tovmassian, G., Zharikov, S., & Neustroev, V. 2012, *Mem. Soc. Astron. Italiana*, 83, 713
- Tovmassian, G. H., Zharikov, S. V., & Neustroev, V. V. 2007, *ApJ*, 655, 466